WILEY-VCH

Ultrafast Spin Current Excitation and Controlled Terahertz Radiation from Noncollinear Antiferromagnets

Yiwen Song[1], Dennis J. X. Lin[2], Shanshan Hu[1], Ziyang Li[1], Jiali Zhang[1], Bee Chun Lim[2], Hnin Yu Yu Ko[2], Shaohai Chen[2], Pin Ho[2*], Qingyuan Jin[1*], Zongzhi Zhang[1*]*

1) Shanghai Ultra-Precision Optical Manufacturing Engineering Research Center and Key Laboratory of Micro and Nano Photonic Structures (MOE), School of Information Science and Technology, Fudan University, Shanghai 200433, China

2) Institute of Materials Research & Engineering, Agency for Science, Technology & Research (A*STAR), 138634 Singapore

E-mail: chen_shaohai@imre.a-star.edu.sg, hopin@imre.a-star.edu.sg, qyjin@fudan.edu.cn, zzzhang@fudan.edu.cn.

Keywords: noncollinear antiferromagnets, magnetic dipole transition, magnetic point group, THz emission, inverse spin Hall effect

Abstract

Noncollinear antiferromagnets (AFMs) are promising candidates for next-generation spintronic devices due to their terahertz (THz) magnetic resonance, robustness against external field interferences, and strong magneto-optical responses. Using femtosecond laser excitation, we systematically investigate spin current generation and THz radiation mechanisms via inverse spin Hall effect in Mn_3Ga/Pt bilayers with multiple magnetic phases. Our results reveal that spin currents in ferrimagnetic Mn_3Ga originate from common hot electron excitation. In contrast, the stronger THz fields from samples containing both ferrimagnetic and noncollinear AFM phases are field-independent, with spin currents arising from pulsed magnetizations through magnetic dipole transitions, observed exclusively in the AFM phase. Furthermore, theoretical models incorporating magnetic group symmetry and nonlinear optical effects are developed, offering accurate explanations for the THz filed dependence on sample azimuth, pump polarization, and pump helicity. These findings open new avenues for generating ultrafast spin currents in noncollinear AFMs, presenting significant potential for high-speed spintronic applications.

1. Introduction

Antiferromagnets (AFMs) are characterized by their zero net magnetization and strong exchange interactions among adjacent spins. The precession frequency of AFMs can reach terahertz (THz) levels, several orders of magnitude higher than that of ferromagnets (FMs).[1, 2] Such advantages make AFMs highly promising for high-speed, high-density, and energy-efficient spintronic memory and computing applications, where spin currents play a crucial role. Time domain THz emission spectroscopy has emerged as a powerful tool for monitoring spin currents and has been extensively investigated in ferromagnet/heavy-metal (FM/HM) and ferrimagnet/heavy-metal (FiM/HM) bilayer structures.[3-5] In these systems, femtosecond (fs) laser interactions with the magnetization of FM or FiM layers generate spin currents on a picosecond (ps) time scale through spin-dependent superdiffusive transport of photoexcited hot electrons.[6, 7] These spin-polarized currents are subsequently converted into transverse impulsive charge currents via the inverse spin Hall effect (ISHE)[8-11] or, more recently through the inverse orbital Hall effect from the orbital currents,[12-16] resulting in electromagnetic wave emissions in the THz frequency range.

The mechanisms governing fs laser-induced spin currents in AFMs fundamentally differ from those in FMs. In the absence of net magnetization and external magnetic fields, two primary mechanisms have been identified. The first involves the generation of pulsed magnetization at THz frequencies via impulsive stimulated Raman scattering (ISRS),[17] which induces ultrafast spin currents through transfer of angular momentum. The second mechanism is driven by phonon–spin interactions, where ultrafast strain pulses in films lead to the formation of transient antiferromagnetic (AF) magnons.[18] Spin current generation via ISRS has been observed in the collinear AFM system of NiO/Pt, relying on the threefold symmetry axis of NiO.[17] Similarly, picosecond spin currents have been reported in the antiferromagnet Cr_2O_3, attributed to optically-excited transient magnetic moments formed at the vicinal metal/Cr_2O_3 interface through interfacial symmetry breaking and interfacial nonlinear magnetic-dipole (MD) transitions.[19]

Recent research has brought noncollinear AFMs of Mn_3X (X = Pt, Ir, Sn, Ga, Ge) into focus due to their high electrical writability and electro-optical readability.[20, 21] Strong anisotropic spin Hall effect,[22, 23] anomalous Hall effect,[24] and tunneling magnetoresistance[25] have been observed in cubic Mn_3Ir and Mn_3Pt with chiral spin ordering. Meanwhile, Weyl semimetal AFMs with hexagonal structures, such as Mn_3Sn, Mn_3Ge, and Mn_3Ga, have gained significant attention for their nontrivial energy bands. Various experiments on the large anomalous Hall effect,[26, 27] anomalous Nernst effect,[28] nonlinear magneto-optical effect,[29]

and laser-induced photon drag effect[30] have provided valuable insights into the ultrafast responses of hexagonal AFMs upon photoexcitation. Laser-induced ultrafast charge currents for THz emission have been reported in the noncollinear AFM Mn_3Sn, which could arise from the dynamics of local magnetic moments[31] or magnetic dipole radiation[32]. Nevertheless, it was found that when Mn_3Sn was capped with Pt, the THz signal was significantly enhanced due to the generation of superdiffusive spin currents from the weak magnetization and the spin-to-charge conversion via ISHE. However, despite these advancements, the mechanisms underlying laser-induced coherent spin currents in noncollinear AFMs remain poorly understood, requiring further investigation to achieve a comprehensive understanding of spin current generation across various magnetic phases.

Among Mn-based AFMs, Mn_3Ga stands out for its unique structural, magnetic, and transport properties, arising from its multiple magnetic and crystalline phases. These phases encompass collinear AF ordering within a face-centered-cubic (*fcc*) structure, ferrimagnetic ordering in a tetragonal structure (τ-phase), and noncollinear AF ordering in a hexagonal structure (ε-phase). This rich diversity in magnetic phases makes Mn_3Ga an excellent candidate for the exploration of nonlinear magneto-optical effects and spin current generation mechanisms. In this study, fs laser-induced anisotropic spin currents are observed at room temperature in Mn_3Ga films with different phases, without requiring the application of an external magnetic field. We demonstrate that spin currents are converted into charge currents within the THz frequency range through the ISHE. Our observations reveal that the strength of the THz electric field emitted from Mn_3Ga/Pt in the presence of ε-phase is highly sensitive to the sample azimuth orientations and laser polarization directions, driven by MD transitions in ε-Mn_3Ga through the magnetic difference-frequency generation process. Conversely, τ-Mn3Ga/Pt samples exhibit a weaker dependence on laser polarization. Moreover, with the THz emission spectroscopy, the magnetic point group symmetries of collinear and noncollinear Mn_3Ga are elucidated. These findings provide deeper insights into transient spin current generation mechanisms in noncollinear AFMs, advancing their potential for multifunctional applications in ultrafast spintronic devices.

2. Result and Discussion

2.1. Crystal structure characterization and THz emission measurements

As shown in **Figure 1**a, ε-Mn_3Ga has a hexagonal crystal structure, characterized by double layers of Mn triangles stacked along the *c*-axis. Within each layer, Mn atoms form a kagome lattice, with Ga atoms located at the centers of the hexagons. Below the Néel

temperature, Mn spins align in the *a*-*b* plane in a triangular AF order, with neighboring spins separated by 120°. The τ-Mn_3Ga phase, depicted in Figure 1b, adopts a tetragonal crystal structure. In this study, it features two Mn sublattices coupled antiferromagnetically along the *c*-axis, resulting in a ferrimagnetic order. Thin films of τ-Mn_3Ga and mixed-phase ε+τ-Mn_3Ga were grown on 0.5-mm-thick MgO (001) substrates and capped with a 5 nm Pt or Al layer.[33] The crystal structures were characterized by X-ray diffraction (XRD), as shown in Figure 1c. For the τ-Mn_3Ga/Pt film, the XRD peak at $2\theta = 46.03°$ corresponds to the tetragonal (103) plane, indicating that the *c*-axis (and spin orientation) is tilted at 72° relative to the film plane. In contrast, for the ε+τ-Mn_3Ga/Pt film, two XRD peaks at 44.72° and 49.35° correspond to the ε-Mn_3Ga (002) and τ-Mn_3Ga (004) planes, respectively. The magnetic hysteresis loop presented in Figure S1 provides further evidence of the ferrimagnetic properties of the τ-Mn_3Ga/Pt sample, as well as the AF characteristics of the ε+τ-Mn_3Ga/Pt films.

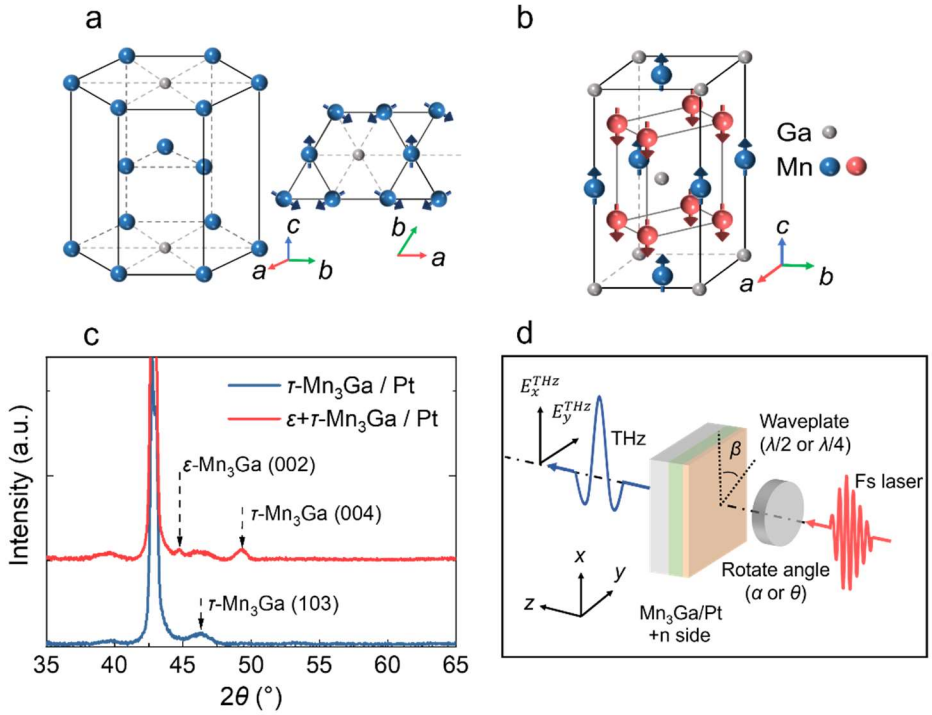

Figure 1. The crystal structure and experimental setup. a) Crystallographic cell of ε-Mn_3Ga. Within each cell, two layers of Mn and Ga atoms are arranged along the *c*-axis direction (left). Kagome lattice within the *a*-*b* plane with arrows indicating the magnetic moments at each Mn site (right). The triangular arrangement of Mn atoms in the *a*-*b* plane forms a noncollinear AF configuration. b) Crystallographic cell of τ-Mn_3Ga, which exhibits a collinear ferrimagnetic magnetic structure. c) The XRD pattern of the MgO (001)/τ-Mn_3Ga (10 nm)/Pt (5 nm) and MgO (001)/ε+τ-Mn_3Ga (25 nm)/Pt (5 nm) films. d) Schematic of the THz emission spectroscopy setup. The sample is positioned in the *x*-*y* plane, and the pump laser pulse propagates along the *z*-direction, with the laser incident from the Pt side labeled as the

+n side incidence. The angle α, θ, and β refer to the linear polarization direction, the rotation angle of the QWP, and the sample azimuth angle, respectively.

The transient spin current response of Mn_3Ga films under fs laser irradiation was investigated using time-domain THz emission spectroscopy. The experimental configuration, schematically illustrated in Figure 1d, assumes the thin films lie in the x–y plane. Linearly or circularly polarized fs laser pulses (800 nm wavelength) were incident normal to the sample plane along the z-axis. Laser incidence from the film side is defined as the +n direction, and from the substrate side as the –n direction. The emitted THz electric fields were passed through two wire grid linear polarizers to separate the parallel (E_x^{THz}) and perpendicular (E_y^{THz}) components relative to the x-axis. The in-plane orientation where E_x^{THz} reaches its maximum is defined as the zero position of the azimuthal angle ($\beta = 0$). By rotating the half-wave ($\lambda/2$) plate (HWP), the linear polarization direction of the incident light can be changed, with the polarization angle of α = 0 aligned parallel to the y-axis. The helicity of the pump laser is controlled by rotating the quarter-wave ($\lambda/4$) plate (QWP) angle θ. Unless otherwise specified, no external magnetic field was applied during the THz emission measurements.

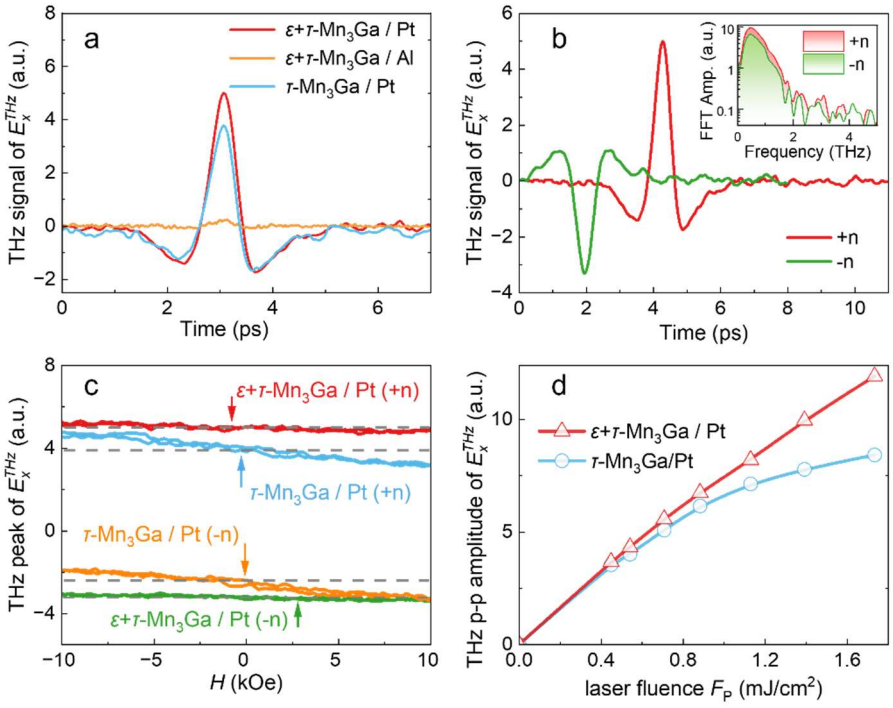

Figure 2. Effects of different crystal structures and normal metal layers. a) Comparison of the THz signals of ε+τ-Mn_3Ga /Pt, ε+τ-Mn_3Ga /Al, and τ-Mn_3Ga /Pt films. b) THz emission from ε+τ-Mn_3Ga/Pt with different incidence directions. As the sample is reversed around the y-axis (-n scenario), THz emission waveforms have the opposite polarity. The inset shows the corresponding THz frequency domain spectrum. c) Influence of the magnetic field on the THz emission from the ε+τ-Mn_3Ga/Pt and

τ-Mn_3Ga/Pt in the +n and -n scenario. The dashed line is the reference value at zero field. d) Variation of the THz amplitude with the pump fluence for ε+τ-Mn_3Ga/Pt and τ-Mn_3Ga/Pt films.

Figure 2a presents the THz waveforms of the E_x^{THz} component measured at the azimuthal angle of β = 0°, with laser incidence from the +n side. Both the τ-Mn_3Ga /Pt and ε+τ-Mn_3Ga /Pt samples exhibit significant THz radiation. In contrast, the ε+τ-Mn_3Ga sample capped with Al produces a negligible THz signal, revealing the critical role of the HM Pt layer. Given the significantly larger spin Hall angle of Pt compared to Al,[34] the observed THz emission is attributed to spin-to-charge conversion (SCC) via the ISHE, driven by ultrafast spin currents generated in Mn_3Ga. To confirm the SCC mechanism, the laser incidence is switched from the film side (+n) to the MgO substrate side (–n) by flipping the sample around the *y*-axis, while maintaining the magnetization orientation of the *y*-component (M_y). As shown in Figure 2b, for the ε+τ-Mn_3Ga/Pt films, the polarity of the THz waveform is reversed. The variation in THz amplitude originates from the absorption of the 800 nm femtosecond laser. Additionally, the time delay between THz signal peaks is due to the group velocity mismatch of THz fields within the MgO substrate.[35] Additionally, the central frequency of 0.6 THz observed in the fast Fourier transform spectra, shown in the inset, further supports the SCC mechanism.[5] For the sample of τ-Mn_3Ga/Pt , the polarity of the THz emission undergoes the same sign changes when the sample is rotated around the *y*-axis (see in Figure S2). All these observations are consistent with the typical THz emission mechanism of SCC in FM (or FiM)/HM systems.

To explore the origin of laser-excited spin currents, we examined the THz peak dependence on the external magnetic field (H) oriented along the *y*-axis and the pump laser fluences (F_P). As shown in Figure 2c, for both the ε+τ-Mn_3Ga/Pt and τ-Mn_3Ga/Pt samples, the polarities remain unchanged as H varies from +10 to -10 kOe. Moreover, unlike the constant peak value of ε+τ-Mn_3Ga/Pt, τ-Mn_3Ga/Pt exhibits slight variations as H varies, characterized by a constant magnitude superimposed with a weak field-dependent signal and identical slopes for +n and -n laser incidence. Figure 2d shows that as F_P increases, the THz peak-to-peak (p-p) amplitude of the ε+τ-Mn_3Ga/Pt sample increases proportionally, with no saturation observed within the energy range of the interest. In contrast, the τ-Mn_3Ga/Pt sample displays a nonlinear trend, which is indicative of a saturable absorption, likely attributed to laser-induced heating and spin accumulation effects.[36, 37] The correlation between the THz field by hot electrons and laser intensity can be described by $E_x^{THz} \propto F_P / \left(F_P + F_{sat}\right)$,[38] where F_{sat} denotes the saturation energy density. For the τ-Mn_3Ga/Pt, F_{sat} is determined to be 0.82 mJ/cm^2. These distinctly different THz amplitude dependencies on magnetic fields and laser fluences suggest that the

underlying mechanisms driving generation of spin currents differ between the ε+τ-Mn_3Ga/Pt and τ-Mn_3Ga/Pt films.

A possible source of spin currents arises from uncompensated magnetizations, as observed in FM/HM and FiM/HM systems. When femtosecond laser pulses irradiate the heterostructure, superdiffusive spin currents are generated through the spin-dependent transport of nonequilibrium hot electrons excited well above the Fermi energy. In such cases, the spin currents, and consequently the THz emission, exhibit saturation with increasing laser fluence, consistent with the observations in Figure 2d for the ferrimagnetic τ-Mn_3Ga (103) sample. In this sample, the easy axis is tilted, resulting in an in-plane magnetization component **M** that could serve as a source of ultrafast superdiffusive spin currents $\boldsymbol{j}_s$, which are responsible for the measured charge current $\boldsymbol{j}_c$, as described by $\boldsymbol{j}_c \propto \theta_{SH}\boldsymbol{j}_s \times \mathbf{M}/|\mathbf{M}|$,[39] where θ_{SH} represents the spin Hall angle. As the magnetic field increases, the in-plane magnetization component grows slightly, leading to the weak dependence of $\boldsymbol{j}_c$, and hence the THz emission on H observed as blue and orange lines in Figure 2c. In contrast, for the ε+τ-Mn_3Ga sample, the Mn spins in the (004)-textured τ-Mn_3Ga phase are oriented perpendicular to the film plane, contributing no detectable THz emission via the ISHE. Furthermore, in the (002)-textured ε-Mn_3Ga phase, the Mn spins are aligned antiferromagnetically within the film plane, leading to zero net magnetization, which prevents the generation of spin currents from uncompensated magnetization.

As a result, we infer that the transient spin currents contributing to the total THz emission in the ε+τ-Mn_3Ga/Pt sample are most likely generated through an alternative mechanism involving the creation of pulsed magnetization via the MD transition. The MD difference-frequency generation is an inelastic scattering process that results in a loss of photon angular momentum. In second-order nonlinear optical processes, even in the absence of an external magnetic field, a transient magnetization $\mathbf{M}(\Omega)$ with a THz frequency of Ω can be excited in AFMs through the MD transition:

$$\mathbf{M}(\Omega) \propto \chi^{(2)}\mathbf{E}(\Omega-\omega)\mathbf{E}(\omega), \quad (1)$$

where $\mathbf{E}(\Omega\text{-}\omega)$ and $\mathbf{E}(\omega)$ are the electric fields of the pump laser at frequencies Ω-ω and ω, respectively, and $\chi^{(2)}$ is the third-rank axial tensor that depends on the symmetries of the crystal and magnetic structures. The magnetization tensor generated by the MD transition can be decomposed into time-symmetric (i-type, $\chi^{(i)}$) and time-antisymmetric (c-type, $\chi^{(c)}$) components, expressed as $\chi^{(2)} = \chi^{(i)} + \chi^{(c)}$,[40] which correspond to crystallographic and spin-dependent contributions, respectively. For ε-Mn_3Ga and τ-Mn_3Ga, the components of $\chi^{(i)}$ and $\chi^{(c)}$ are uniquely defined by their respective crystallographic and magnetic structures. The tetragonal

Mn_3Ga is characterized by the space group *I*4/*mmm* (No.139), corresponding to the magnetic point group 4/*mm*'*m*'. It is important to note that for the point group 4/*mm*'*m*', the allowed fundamental symmetry operations include -1, 4_z, and C_{2y}', while the pulsed magnetization induced by the intense fs laser is prohibited within the *x*-*y* plane. Consequently, the measured THz emission in *τ*-Mn_3Ga/Pt is not associated with nonlinear optical effects, but instead arises from the spin-dependent superdiffusion of the nonequilibrium hot electrons, with the in-plane net magnetization component playing a key role.

In contrast, hexagonal Mn_3Ga belongs to the crystal space group $P6_3/mmc$ (No.194) when magnetization is not considered. However, when accounting for the AF properties stabilized within the temperature range of approximately 250–420 K, it is described by the magnetic point group *m*'*m*'*m* with fundamental symmetry operators including C_{2x}', C_{2y}, and C_{2z}',[41] which facilitates fs-induced MD transitions. For pump laser incident along the *z*-axis, the nonzero nonlinear susceptibility elements are $\chi_{xyx} = \chi_{xxy}$, χ_{yyy} and χ_{yxx}. The pulsed magnetization **M** excited by the second-order nonlinear effect can be expressed as:

$$\begin{pmatrix} M_x \\ M_y \end{pmatrix} \propto \begin{pmatrix} 2\chi^{(2)}_{xxy} E_x E_y \\ \chi^{(2)}_{yxx} E_x^2 + \chi^{(2)}_{yyy} E_y^2 \end{pmatrix}. \quad (2)$$

According to **Equation 1**, the THz amplitude is expected to be proportional to the laser fluence, which aligns well with the linear increase observed in Figure 2d. This agreement indicates that, for the *ε*+*τ*-Mn_3Ga/Pt sample, the nonlinear optical effect predominantly governs the THz emission via pulsed magnetization. Moreover, the MD transition in *ε*+*τ*-Mn_3Ga/Pt is notably strong, with its THz amplitude surpassing that of the ferrimagnetic *τ*-Mn_3Ga/Pt sample, where spin currents are produced by hot electron excitation. Given that the electro-optical signal is proportional to **M**, we next establish the relationship between the detected THz electric signal and various measurement conditions, including the sample azimuth, the polarization angle of the linear pump beam, and the pump helicity.

2.2. The impacts of sample azimuthal angle and linear polarization of laser

To further understand the magneto-optic interaction processes within the Mn_3Ga layer, we investigated the dependence of the THz p-p amplitude on the azimuthal angle *β*. As shown in **Figure 3**a, for the *τ*-Mn_3Ga/Pt bilayer, the p-p amplitude of E_x^{THz} exhibits a periodic variation with *β*, with a period of 360°. It reaches extreme values at *β* = 0° and 180°, where the waveform polarity reverses. Conversely, the E_y^{THz} component attains its extreme values at *β* = 90° and 270°, indicating a rotation in the direction of the resultant spin currents as the azimuth angle

rotates within the *x*-*y* plane. For the ε+τ-Mn_3Ga/Pt sample, the dependence on β is depicted in Figure 3b, revealing a similar period relationship for E_x^{THz}. However, the E_y^{THz} component shows significantly smaller amplitudes and opposite polarity. According to **Equation 2**, and through symmetry analysis of the second-order nonlinear susceptibility, the azimuth-dependent THz amplitude of E_x^{THz} is derived to be proportional to $\left[\sin^2\beta\left(\chi_{yxx}+2\chi_{xxy}\right)+\cos^2\beta\chi_{yyy}\right]\cos\beta$, while the E_y^{THz} component is proportional to $\left[\cos^2\beta\left(-\chi_{yyy}+2\chi_{xxy}\right)-\sin^2\beta\chi_{yxx}\right]\sin\beta$ (Supporting Information section S3). The differing values of χ_{xyx}, χ_{yyy}, and χ_{yxx} are responsible for the observed variations in amplitude and polarity of E_x^{THz} and E_y^{THz}.

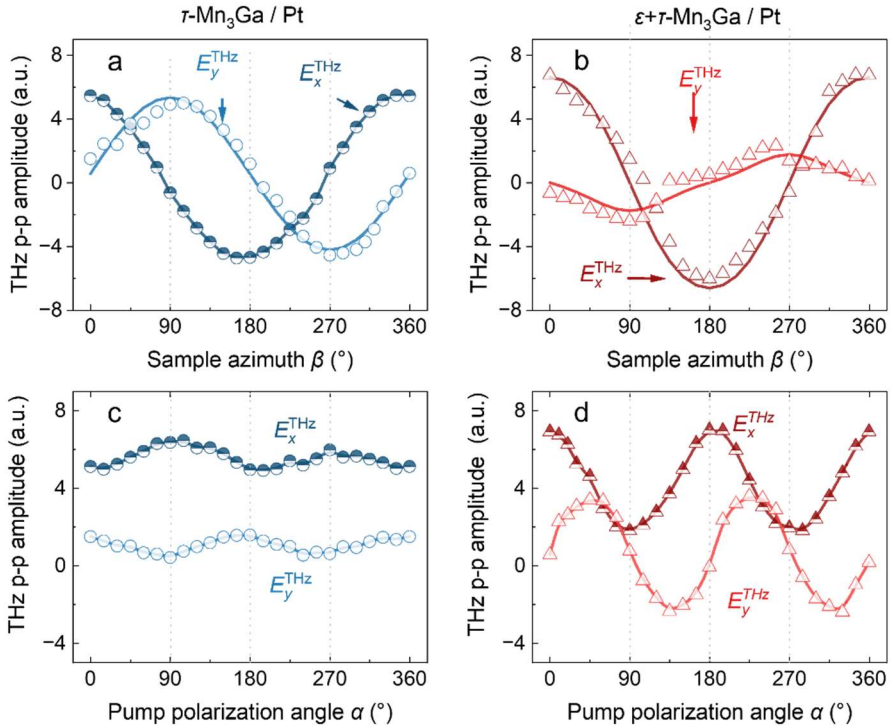

Figure 3. The THz radiation amplitudes of Mn_3Ga/Pt samples under different sample azimuth and pump light polarization angles. The amplitudes of THz emission (E_x^{THz} and E_y^{THz}) from the samples of a) τ-Mn_3Ga/Pt and b) ε+τ-Mn_3Ga/Pt as a function of the azimuth angle β. The THz emission amplitudes (E_x^{THz} and E_y^{THz}) at different laser polarization angles α are summarized in c) for τ-Mn_3Ga/Pt and d) for ε+τ-Mn_3Ga/Pt films.

To further illustrate the existence of multiple sources of spin currents in different phases of Mn_3Ga, we varied the linear polarization angle α of the incident light by rotating a HWP while keeping the sample azimuth fixed at $\beta = 0°$. The dependence of THz emission amplitudes on pump polarization is shown in Figure 3c for the τ-Mn_3Ga/Pt bilayer sample. It is found that

the p-p amplitudes of both E_x^{THz} and E_y^{THz} components are nearly constant, exhibiting only weak oscillations with a periodicity of 180°. This isotropic dependence on α is consistent with the hot electron superdiffusion mechanism for spin current generation in τ-Mn_3Ga/Pt, while the quite weak polarization-dependent anisotropic oscillations are attributed to the magnetization-induced optical rectification effect, a phenomenon observed in FM/HM systems.[42]

In contrast, the THz emission driven by the MD transition mechanism shows a strong dependence on the polarization angle, as described by $E_x^{THz} \propto \chi_{yxx} + \left(\chi_{yyy} - \chi_{yxx}\right)\sin^2\alpha$ and $E_y^{THz} \propto \chi_{xxy}\sin 2\alpha$ at $\beta = 0°$ (Supporting Information section S3). Figure 3d displays the THz amplitudes for the ε+τ-Mn_3Ga/Pt sample as a function of the laser polarization angle α. As expected, both E_x^{THz} and E_y^{THz} components exhibit a prominent sinusoidal dependence on α, with a periodicity of 180° and a phase difference of 45°. The large anisotropic contribution allows for significant modulation of THz radiation intensity by varying the pump polarization angle over a range of 90°. These results are in good agreement with the theoretical predictions, verifying that the polarization state of the transient magnetization aligns with that of the incident laser, a characteristic of the stimulated scattering. By fitting the curves in Figures 3b and 3d, an identical ratio of the nonlinear tensor components is yielded: χ_{xxy}: χ_{xyx}: χ_{yxx}: $\chi_{yyy} \approx 28:28:17:66$. Based on this proportional relationship, the maximum amplitude of the E_y^{THz} component is predicated to be one-third that of E_x^{THz}, which is in accordance with the experimental data shown in Figure 3b.

2.3. The THz emission dependences on the helicity of the pump laser

To clarify the impact of circularly polarized (CP) laser excitation, the helicity of the pump laser was modulated by rotating the QWP to an angle θ. The time-domain THz spectra of E_x^{THz} and E_y^{THz}, pumped by right-handed (+σ, θ = 45°) and left-handed (-σ, θ = 135°) CP light, are presented in **Figure 4**a and Figure 4b, respectively, for the ε+τ-Mn_3Ga/Pt bilayers at $\beta = 0$. The E_x^{THz} exhibits a comparable THz peak with the same polarity, regardless of whether the excitation is with +σ or -σ light, while the E_y^{THz} waveform displays an opposite polarity.

To clarify the helicity dependent THz emission in the ε+τ-Mn_3Ga/Pt film, the p-p amplitudes of E_x^{THz} and E_y^{THz} are summarized in Figure 4c and Figure 4d as a function of the QWP angle. According to the deduced theoretical formula, the components of the linear polarization dependence are related to the real part of the nonlinear susceptibility. In this context,

the E_x^{THz} component is expected to be proportional to $-\chi_{yxx}\sin^2 2\theta$ and the E_y^{THz} proportional to $\sin 2\theta\cos 2\theta\chi_{xxy}$, both exhibiting fourfold symmetry. However, the curve in **Figure 4d** deviates from this expected behavior, indicating that spin current generation cannot be solely attributed to linearly polarized laser excitation. To distinguish the contributions from the linear and circular polarization pump lasers, we performed a quantitative analysis using a phenomenological formula:[43]

$$E^{THz} = L_1 \sin 4\theta + L_2 \cos 4\theta + C \sin 2\theta + D, \quad (3)$$

where L_1 and L_2 represent the contributions from the linearly polarized pump, while the term involving C accounts for the contribution from the CP light. The last term D corresponds to the signal that is independent of laser polarization state. The fitted parameters are presented in the insets of Figures 4c and 4d. Notably, the helicity-dependent THz field is primarily emitted along the E_y^{THz} direction, as indicated by the dominant coefficient C presented in the inset of Figure 4d. The observation of helicity-dependent **M** is consistent with the inverse Faraday effect. It is important to note that, for the τ-Mn_3Ga/Pt system, where the spin current is thermally excited, the dependence of THz emission on the pump laser helicity is negligible (see Figure S3, Supporting Information).

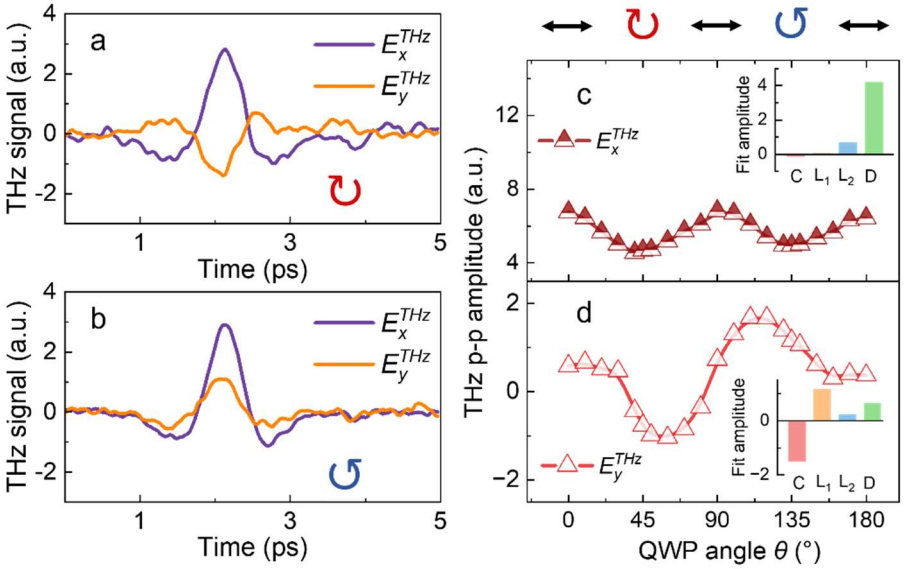

Figure 4. Dependence of THz electric field components on the laser helicity for the ε+τ-Mn_3Ga/Pt sample. a) and b) show the waveforms of E_x^{THz} and E_y^{THz} under right-handed CP laser excitation (+σ, θ = 45°) and left-handed CP laser excitation (-σ, θ = 135°), respectively. c) and d) are the summarized p-

p amplitudes of the E_x^{THz} and E_y^{THz} as a function of the QWP angle θ. The insets show the fitted contributions corresponding to the different polarization states.

3. Conclusion

In summary, our research identifies optically excited spin currents in Mn_3Ga, encompassing both the tetragonal FiM and hexagonal noncollinear AFM phases, at zero magnetic field and room temperature. The pulsed magnetization generates picosecond spin currents and THz radiation via the ISHE, with coherent excitation being exclusively observed in the noncollinear AFM Mn_3Ga. We attribute the generation of spin currents in the noncollinear AFM phase to the MD transition, which arises from the inversion symmetry breaking of the magnetic point group. By considering magnetic symmetry and nonlinear optical effects, the MD transition process in the noncollinear AFM is accurately modeled. A distinct dependence of the THz emission on the laser polarization and sample azimuth angles is observed, aligning well with our theoretical predictions. Furthermore, helicity-dependent spin currents are detected upon excitation with CP light, attributed to the inverse Faraday effect. In contrast, spin currents in the tetragonal FiM Mn_3Ga result from spin-dependent superdiffusion of excited nonequilibrium hot electrons, exhibiting negligible dependence on the polarization and helicity of the pump lasers. This work provides a promising pathway for generating and modulating transient spin currents in noncollinear AFM materials through the second-order MD transitions, paving the way for the practical applications of AFM dynamics in ultrafast spintronics.

4. Experimental Section

Sample Deposition: Thin film heterostructures comprising Mn_3Ga (10 or 25) nm and Al or Pt (5 nm) were fabricated using a Chiron^{TM} magnetron physical vapor sputtering system, deposited onto 1 × 1 cm^2 (001) MgO substrates at controlled temperatures. The chamber was maintained at a base pressure of < 1 × 10^{-8} Torr, with a working pressure of 1.6 × 10^{-3} Torr under an ionized Ar^+ atmosphere during deposition. The Mn_3Ga layer was sputtered from a 2-inch composite target with an atomic stoichiometry of $Mn_{75}Ga_{25}$ at a calibrated rate of 2.59 nm/min, whilst Al and Pt cap layers were fabricated from 2-inch elemental targets at rates of 1.60 and 2.80 nm/min, respectively. All deposition rates were measured using atomic force microscopy (AFM, Veeco 3100). Substrate temperatures (T_s) of room temperature (RT), 200, 350, and 500 °C were set using a pre-bake and maintained during Mn_3Ga sputtering, yielding τ-Mn_3Ga (350 °C) and ε+τ-Mn_3Ga (500 °C) films. All cap layers were deposited at RT.

THz emission measurement: THz emission measurements were performed using a commercial Ti:sapphire laser (central wavelength of 800 nm, pulse duration of 50 fs, and repetition frequency of 1 kHz). The laser beam was split into two parts (at a 9:1 intensity ratio) for excitation and detection of the THz electric field, with the pump pulse incident perpendicular to the film surface along the *z*-axis. The laser beam incident on the sample surface had a spot diameter of approximately 3 mm. Two wire grids were used to polarize the THz waves, dividing the generated THz electric field into two orthogonal components. The radiated THz beams were focused onto a 1-mm-thick <110> ZnTe crystal using two 90° off-axis parabolic mirrors. The encoded THz electric signal was then extracted via electro-optic sampling in the time domain by controlling the delay between the pump and probe pulses. To reduce the THz absorption by water molecules, the measurements were conducted in a dry environment with humidity below 8%.

Supporting Information

Supporting Information is available from the Wiley Online Library or from the author.

Acknowledgements

This work is supported by the National Natural Science Foundation of China (Grant Nos. 12374104, 52171230, 11874120, and 12074072), and by the RIE2025 Manufacturing, Trade and Connectivity (MTC) Individual Research Grant (Grant No. M23M6c0101) and Career Development Fund (Grant No. C210812017), administered by A*STAR.

References

[1] R. Cheng, D. Xiao, A. Brataas, *Phys. Rev. Lett.* **2016**, 116, 207603.
[2] L. Huang, Y. Cao, H. Qiu, H. Bai, L. Liao, C. Chen, L. Han, F. Pan, B. Jin, C. Song, *Nat. Commun.* **2024**, 15, 7227.
[3] Z. Ji, Y. Song, Y. Song, Z. Li, J. Zhang, S. Lou, Z. Zhang, Q. Jin, *ACS Appl. Mater. Interfaces* **2024**, 16, 24075.
[4] M. Chen, R. Mishra, Y. Wu, K. Lee, H. Yang, *Adv. Opt. Mater.* **2018**, 6, 1800430.
[5] T. Seifert, S. Jaiswal, U. Martens, J. Hannegan, L. Braun, P. Maldonado, F. Freimuth, A. Kronenberg, J. Henrizi, I. Radu, E. Beaurepaire, Y. Mokrousov, P. M. Oppeneer, M. Jourdan, G. Jakob, D. Turchinovich, L. M. Hayden, M. Wolf, M. Münzenberg, M. Kläui, T. Kampfrath, *Nat. Photon.* **2016**, 10, 483.
[6] M. Battiato, K. Carva, P. M. Oppeneer, *Phys. Rev. Lett.* **2010**, 105, 027203.
[7] Z. Ji, Y. Song, Y. Liu, Y. Zhang, Z. Li, Y. Song, J. Zhang, S. Lou, Z. Zhang, Q. Jin, *Appl. Phys. Lett.* **2023**, 123.

[8] J. Jechumtál, R. Rouzegar, O. Gueckstock, C. Denker, W. Hoppe, Q. Remy, T. S. Seifert, P. Kubaščík, G. Woltersdorf, P. W. Brouwer, M. Münzenberg, T. Kampfrath, L. Nádvorník, *Phys. Rev. Lett.* **2024**, 132, 226703.
[9] P. Agarwal, Y. Yang, R. Medwal, H. Asada, Y. Fukuma, M. Battiato, R. Singh, *Adv. Opt. Mater.* **2023**, 11, 2301027.
[10] A. Kefayati, B. K. Nikolić, *Phys. Rev. Lett.* **2024**, 133, 136704.
[11] F. Foggetti, P. M. Oppeneer, *Phys. Rev. Appl.* **2025**, 23, 014067.
[12] Y. Xu, F. Zhang, A. Fert, H.-Y. Jaffres, Y. Liu, R. Xu, Y. Jiang, H. Cheng, W. Zhao, *Nat. Commun.* **2024**, 15, 2043.
[13] S. S. Mishra, J. Lourembam, D. J. X. Lin, R. Singh, *Nat. Commun.* **2024**, 15, 4568.
[14] S. Kumar, S. Kumar, *Nat. Commun.* **2023**, 14, 8185.
[15] P. Wang, Z. Feng, Y. Yang, D. Zhang, Q. Liu, Z. Xu, Z. Jia, Y. Wu, G. Yu, X. Xu, Y. Jiang, *npj Quantum Mater.* **2023**, 8, 28.
[16] T. S. Seifert, D. Go, H. Hayashi, R. Rouzegar, F. Freimuth, K. Ando, Y. Mokrousov, T. Kampfrath, *Nat. Nanotechnol.* **2023**, 18, 1132.
[17] H. Qiu, L. Zhou, C. Zhang, J. Wu, Y. Tian, S. Cheng, S. Mi, H. Zhao, Q. Zhang, D. Wu, B. Jin, J. Chen, P. Wu, *Nat. Phys.* **2021**, 17, 388.
[18] E. Rongione, O. Gueckstock, M. Mattern, O. Gomonay, H. Meer, C. Schmitt, R. Ramos, T. Kikkawa, M. Mičica, E. Saitoh, J. Sinova, H. Jaffrès, J. Mangeney, S. T. B. Goennenwein, S. Geprägs, T. Kampfrath, M. Kläui, M. Bargheer, T. S. Seifert, S. Dhillon, R. Lebrun, *Nat. Commun.* **2023**, 14, 1818.
[19] B. Yang, Q. Ji, F. Z. Huang, J. Li, Y. Z. Tian, B. Xue, R. Zhu, H. Wu, H. Yang, Y. B. Yang, S. Tang, H. B. Zhao, Y. Cao, J. Du, B. G. Wang, C. Zhang, D. Wu, *Phys. Rev. Lett.* **2024**, 132, 176703.
[20] S. Chen, D. J. X. Lin, B. C. Lim, P. Ho, *J. Phys. D.* **2024**, 57.
[21] B. H. Rimmler, B. Pal, S. S. P. Parkin, *Nat. Rev. Mater.* **2024**.
[22] C. Cao, S. Chen, R.-C. Xiao, Z. Zhu, G. Yu, Y. Wang, X. Qiu, L. Liu, T. Zhao, D.-F. Shao, Y. Xu, J. Chen, Q. Zhan, *Nat. Commun.* **2023**, 14, 5873.
[23] J. Železný, Y. Zhang, C. Felser, B. Yan, *Phys. Rev. Lett.* **2017**, 119, 187204.
[24] Z. Q. Liu, H. Chen, J. M. Wang, J. H. Liu, K. Wang, Z. X. Feng, H. Yan, X. R. Wang, C. B. Jiang, J. M. D. Coey, A. H. MacDonald, *Nat. Electron.* **2018**, 1, 172.
[25] P. Qin, H. Yan, X. Wang, H. Chen, Z. Meng, J. Dong, M. Zhu, J. Cai, Z. Feng, X. Zhou, L. Liu, T. Zhang, Z. Zeng, J. Zhang, C. Jiang, Z. Liu, *Nature* **2023**, 613, 485.
[26] X. Li, J. Koo, Z. Zhu, K. Behnia, B. Yan, *Nat. Commun.* **2023**, 14, 1642.
[27] L. Song, F. Zhou, H. Li, B. Ding, X. Li, X. Xi, Y. Yao, Y. C. Lau, W. Wang, *Adv. Funct. Mater.* **2024**, 34, 2316588.
[28] M. Ikhlas, T. Tomita, T. Koretsune, M.-T. Suzuki, D. Nishio-Hamane, R. Arita, Y. Otani, S. Nakatsuji, *Nat. Phys.* **2017**, 13, 1085.
[29] H. C. Zhao, H. Xia, S. Hu, Y. Y. Lv, Z. R. Zhao, J. He, E. Liang, G. Ni, L. Y. Chen, X. P. Qiu, S. M. Zhou, H. B. Zhao, *Nat. Commun.* **2021**, 12, 5266.
[30] D. Hamara, G. F. Lange, F. N. Kholid, A. Markou, C. Felser, R.-J. Slager, C. Ciccarelli, *Commun. Phys.* **2023**, 6, 320.
[31] A. Suresh, B. K. Nikolić, *Phys. Rev. B* **2023**, 107, 174421.
[32] X. Zhou, B. Song, X. Chen, Y. You, S. Ruan, H. Bai, W. Zhang, G. Ma, J. Yao, F. Pan, Z. Jin, C. Song, *Appl. Phys. Lett.* **2019**, 115.
[33] S. Chen, D. J. X. Lin, B. C. Lim, H. K. Tan, Y. Y. K. Hnin, S. K. Wong, I. Lim, R. J. J. Lim, K. H. Khoo, P. Ho, *APL Mater.* **2023**, 11, 101126.
[34] J. Sinova, S. O. Valenzuela, J. Wunderlich, C. H. Back, T. Jungwirth, *Rev. Mod. Phys.* **2015**, 87, 1213.
[35] Z. Feng, R. Yu, Y. Zhou, H. Lu, W. Tan, H. Deng, Q. Liu, Z. Zhai, L. Zhu, J. Cai, B. Miao, H. Ding, *Adv. Opt. Mater.* **2018**, 6, 1800965.

[36] D. Yang, J. Liang, C. Zhou, L. Sun, R. Zheng, S. Luo, Y. Wu, J. Qi, *Adv. Opt. Mater.* **2016**, 4, 1944.
[37] Z. Ji, Y. Song, Y. Song, Z. Li, J. Zhang, S. Lou, Z. Zhang, Q. Jin, *ACS Appl. Mater. Interfaces* **2024**, 16, 24075.
[38] Y. Liu, H. Bai, Y. Song, Z. Ji, S. Lou, Z. Zhang, C. Song, Q. Jin, *Adv. Opt. Mater.* **2023**, 11, 2300177.
[39] T. Kampfrath, M. Battiato, P. Maldonado, G. Eilers, J. Nötzold, S. Mährlein, V. Zbarsky, F. Freimuth, Y. Mokrousov, S. Blügel, M. Wolf, I. Radu, P. M. Oppeneer, M. Münzenberg, *Nat. Nanotechnol.* **2013**, 8, 256.
[40] R. R. Birss, *Rep. Prog. Phys.* **1963**, 26, 307.
[41] S.-W. Cheong, F.-T. Huang, *npj Quantum Mater.* **2023**, 8, 73.
[42] Z. Yao, H. Fu, W. Du, Y. Huang, Z. Lei, C. You, X. Xu, *Phys. Rev. B* **2021**, 103, L201404.
[43] J. W. McIver, D. Hsieh, H. Steinberg, P. Jarillo-Herrero, N. Gedik, *Nat. Nanotechnol.* **2012**, 7, 96.

Table of Content

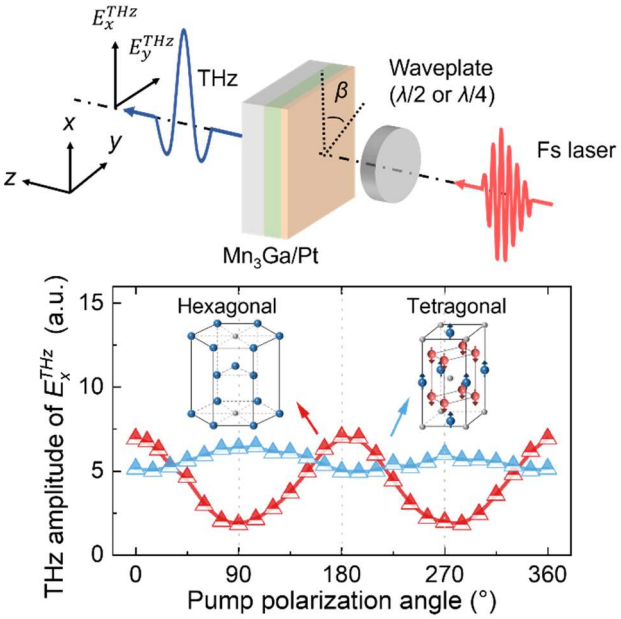

This study employs terahertz spectroscopy to generate ultrafast spin currents and terahertz radiation in Mn_3Ga/Pt bilayers. In the tetragonal ferrimagnetic Mn_3Ga, spin currents arise from hot-electron excitations, whereas in the hexagonal noncollinear antiferromagnetic Mn_3Ga, spin currents are attributed to the anisotropic pulsed magnetization. Magnetic dipole transitions in noncollinear antiferromagnets enable novel strategies for ultrafast antiferromagnetic device applications.